doi:10.3969/j.issn.1673-9736.2019.02.09
Article ID: 1673-9736(2019)02-0133-08

Applications of gravity data in identification of faults and tectonic boundaries of a working area in Inner Mongolia

ZOU Bolun, LI Tonglin, WU Yangang, WU Heyu, SHI Jiaqiang and LIN Baoze

College of Geo-Exploration Science and Technology, Jilin University, Changchun 130026, China

Abstract: In order to determine the tectonic framework of the Late Paleozoic sedimentary basin of the studied area in Inner Mongolia, horizontal derivative, vertical derivative, total gradient modulus, tilt angle, and Euler deconvolution methods were used to process the high-precision gravity data. Four major faults and six secondary faults have been identified according to the horizontal fault position information provided by the first four methods, and the fault depth information were obtained using the Euler deconvolution method. The interpreted faults were identified as the main basin-controlling structures in the study area, which was helpful for deepening the understanding of the basin's structure, as well as providing important references for delineating hidden polymetallic ore veins.

Keywords: gravity; Euler deconvolution; tectonic boundaries; identification; Inner Mongolia

0 Introduction

The Xing'an working area of Inner Mongolia is located between the Siberian Plate and the North China Plate. The NE-trending Sumoqagan Obo-Arun Banner deep fault zone passes through the region (Zhang, 2015). The study area was located in the marginal-Pacific metallogenic region, Daxing'anling metallogenic province, and the East Ujimqin Banner-Nenjiang River-Dobaoshan-Heihe Cu-Mo-Au-Fe-Zn metallogenic subzone, and had previously been identified as having good prospects. Gravity exploration is a type of mature geophysical exploration method and it is often used as the conventional method in geological interpretations and the delineation of fault structures. In this study, the gravity data of the study area were collected and then processed using horizontal derivative, vertical derivative, total gradient modulus, and tilt angle methods. Integrating Euler deconvolution method, the fault and tectonic information of this area was then analyzed, which is the basis for future prospecting and development of other geophysical methods.

1 Geological overview

1.1 Strata and structures

The stratigraphic divisions of the study area belonged to the North Xinjiang-Xing'an stratigraphic region, Xing'an stratigraphic region, and Harbin stratigraphic region of the Paleozoic Period. The outcropped strata consist of Linxi Formation (P_3l), Hadatolegai Formation (T_3hd), Manketou'ebo Formation (J_3mk), Manitou Formation (J_3mn) and Quaternary Sediment (Q) (Liu *et al.*, 2018). The Linxi Formation (P_3l) of the Upper Permian was widely distributed. It was composed of a black-gray sandstone-slate assemblage of lacustrine facies and lagoon facies conformably or unconformably overlying Zhesi Formation. The formation was found to be rich in animal and

Received 5 March 2019, accepted 25 March 2019

plant fossils (Fig. 1) (Xiao *et al.*, 2018).

The fault structures were well developed in the study area and were determined to have mainly been formed during the Late Variscan and Yanshanian. The most prominent regional faults were parallel NE-trending faults. The Yanshanian Movement was considered to have been the strongest tectonic movement in the study area accompanied by a large number of volcanic eruptions and magmatic intrusions, forming the main tectonic framework of the area. This framework, manifested during the large-scale multi-stage continental volcanic activities, consists of two groups of fault structures, sedimentary basins, and basement faults in both NE-NNE and NW directions. The faulting occurred during the Himalayan Period could only be inferred from the landscapes and Quaternary geology, and all them were along the pre-existing faults.

The fold structures in the study area mainly developed within the Late Variscan and Yanshan tectonic layers. It was found that the different tectonic layers displayed different fold structures. For example, the Variscan folds were characterized by open-tight linear anticlines and synclines, with overall NE-NNE trending "S" type bends, whereas the Yanshanian folds mainly developed on the basis of the Late Variscan folds as linear anticlines and synclines in NE direction. Moreover, there were a few NW trending wide-gentle short-axis folds observed, and the regional tectonic traces of that period were not obvious (Xu, 2018).

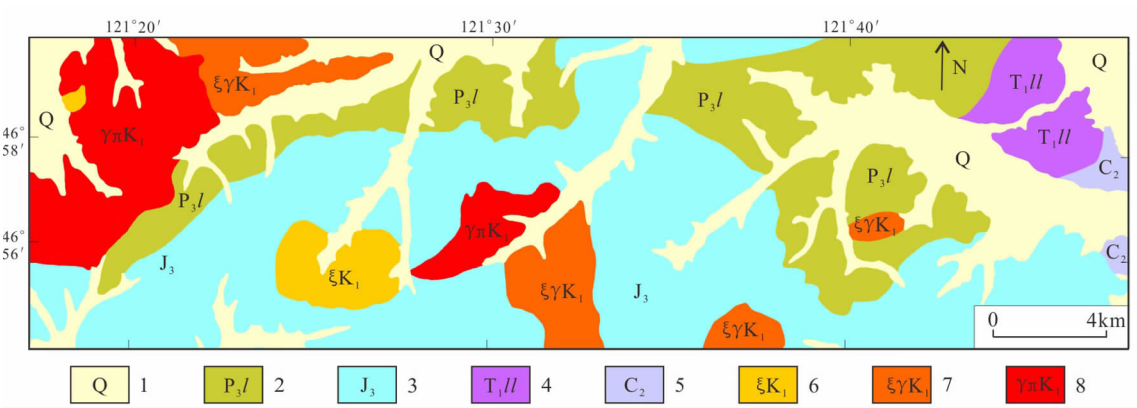

1. Quaternary Holocene; 2. Upper Permian siltstone; 3. Upper Jurassic; 4. Lower Triassic purple sandstone; 5. Middle Carboniferous; 6. Early Cretaceous syenite; 7. Early Cretaceous syengranite; 8. Early Cretaceous granite porphyry.

Fig. 1 Geological map of Jirigen area

2 Identification of faults and tectonic boundaries in the study area

2.1 Horizontal derivatives

In order to examine the distributions of the faults and tectonic boundaries in the study area, a horizontal derivative method was used to process the data. This conventional method was taken as the most effective method in identifying the large dip faults and geological boundaries. The Bouguer gravity anomaly is shown in Fig. 2.

Derivative calculations of gravity anomalies are widely used in the processing and interpretation of anomalies. The reason for this is that the derivatives of anomalies have different characteristics in different geological bodies, which is helpful for the interpretations and classifications of anomalies. Furthermore, the derivatives of anomalies can highlight shallow geological factors and meanwhile suppress the influences of deep geological factors, and can, to a certain extent, differentiate superimposed anomalies produced by field sources of different depths and sizes (Li, 2017).

In accordance with the differential properties of Fourier Transform, the first-order horizontal derivatives of the anomalies along the x and y directions, re-

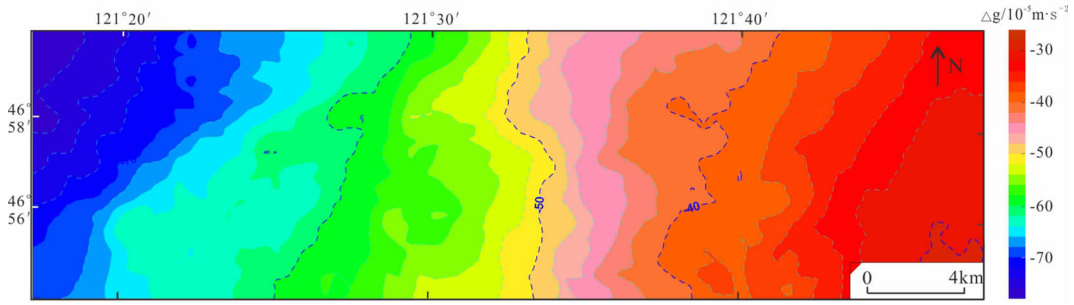

Fig. 2 Bouguer gravity anomaly

spectively, were as follows:

$$\begin{cases} \dfrac{\partial \tilde{T}}{\partial x} = iu\tilde{T} \\ \dfrac{\partial \tilde{T}}{\partial y} = iv\tilde{T} \end{cases} \tag{1}$$

The total horizontal derivative was expressed as:

$$T_h = \sqrt{\left(\frac{\partial T}{\partial x}\right)^2 + \left(\frac{\partial T}{\partial y}\right)^2} \tag{2}$$

The horizontal derivatives can be used to highlight anomalous features in certain directions. In this study, from the wave number response diagram of the theoretical model, it can be seen that the directional derivatives along the X direction can amplify the high-frequency components along the Y direction. Also, the directional derivatives along the Y direction can amplify the high-frequency components along the X direction. Therefore, the horizontal derivatives are often used to analyze the characteristics of structural lines in a certain direction during practical application processes. It is known that the total horizontal derivative has prominent effects on the high-frequency components in any direction.

The co-axis of horizontal derivative contour trap of gravity can identify the boundaries of density changes. Therefore, it can be used to locate the positions of faults. The derivatives of the X and Y directions and the total horizontal derivatives of the Bouguer gravity anomaly following the reduction of the curved surfaces into a horizontal plane were adopted to reflect the distributions of the faults or the density changes of the tectonic lines in the north-south direction, east-west direction, and the entire plane, respectively, as detailed in Fig. 3.

As it can be seen in Fig. 3a-c, the first-order derivative of the "x" direction of the Bouguer gravity anomaly highlighted the structural characteristics of the SN, NNE, and NNW directions. The first-order derivative of the "y" direction highlighted the structural characteristics of EW and NE directions, and the total horizontal derivative indicated that the western structure of the study area was NE-oriented, while the central structure was NNW-oriented.

2.2 Vertical derivatives

In accordance with the differential properties of the Fourier Transform, the formula for calculating the vertical first-order derivatives along the z direction in a wave number domain can be written as follows:

$$\frac{\partial \tilde{T}}{\partial z} = \sqrt{u^2 + v^2}\ \tilde{T} \tag{3}$$

Fig. 3d-e reflects the variation rates of the gravity anomalies along the vertical direction. The background field was suppressed in order to highlight the local anomalies. Then, by applying Formula (3) once again to calculate the vertical first-order derivatives, the spectrum of the vertical second derivatives could be obtained. The zero line of the vertical second derivatives could then be used to approximate the boundaries of the gravity field sources. As detailed in Fig. 4, the range which had been delineated by the zero line of the vertical second derivative was roughly the same as that of the residual gravity anomaly. These findings confirmed that the seperation of the regional residual anomalies were reasonable.

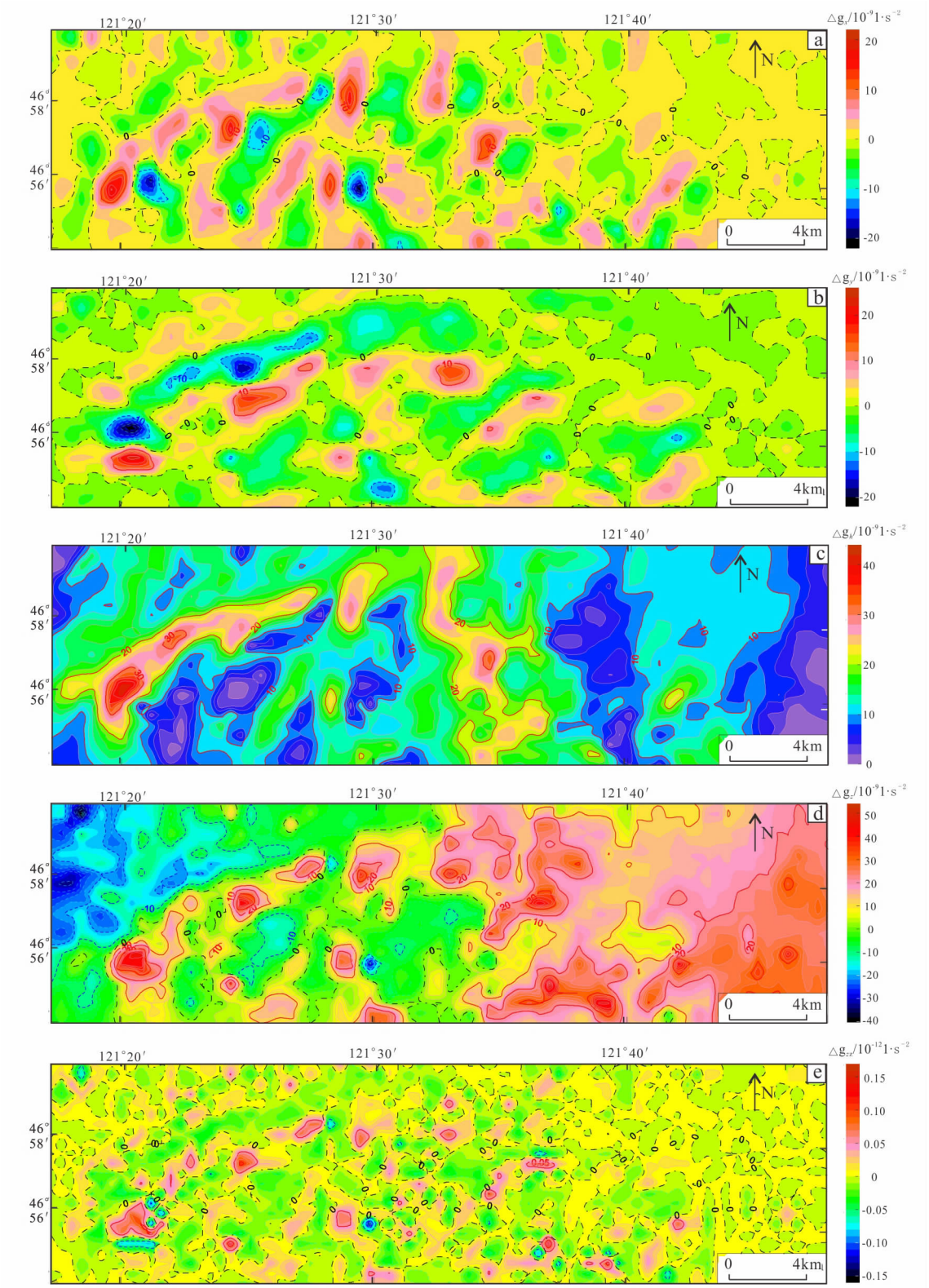

(a) First-order derivative in the *x* direction; (b) first-order derivative in the *y* direction; (c) total horizontal first-order derivative; (d) vertical first-order derivative; (e) vertical second-order derivative.

Fig. 3 Diagrams of horizontal directional derivatives (a, b, c) and vertical derivative results (d, e) of Bouguer gravity anomaly following reduction of curved surfaces into a horizontal plane

2.3 Total gradient modulus

The total gradient modulus (directional analytic signal) is the square root of the sum of squares after calculating the derivatives of the anomalies in different directions. The boundaries or linear structures of the field sources were identified by the maximum value of the total gradient modulus (Zhou *et al.*, 2018; Li *et al.*, 2018; Ren *et al.*, 2017; Zhang *et al.*, 2017; Chen *et al.*, 2017). The amplitude of the total gradient modulus was related to the change rates of the anomalies in the horizontal and vertical directions. Generally, the steeper the horizontal boundary of a field source and the shallower the burial depth are, the larger the amplitude of the total gradient modulus will be, as follows:

$$AS = \sqrt{\left(\frac{\partial T}{\partial x}\right)^2 + \left(\frac{\partial T}{\partial y}\right)^2 + \left(\frac{\partial T}{\partial z}\right)^2} \qquad (4)$$

The total gradient modulus of the local anomaly shown in Fig. 4a indicated that a large number of equiaxed anomalies were distributed in the shallow sections, which is similar to the results of the vertical first-order derivatives of the residual Bouguer anomaly.

2.4 Tilt angle method

Tile angle method is a balanced potential field enhancement method. In this study, the ratio of the vertical derivative to the total horizontal derivative was used to weaken the negative effects of the buried depths of the field sources on the boundary recognitions. The tilt angle method can achieve the effects of positive values inside the field sources, zero values near the boundaries, and negative values outside the field sources. Therefore, the boundaries of the deep and shallow field sources became more balanced as follows:

$$Tilt = \frac{U_{zz}}{\sqrt{U_{xz}^2 + U_{yz}^2}} \qquad (5)$$

The results of the tilt angle of the residual Bouguer anomaly are shown in Fig. 4b. Generally, the regional structure was dominated by a NE-trending structure, and with near SN-trending structures locally.

2.5 Euler deconvolution

The Euler deconvolution method is known to be a fast method for calculating the buried depths of gravity and magnetic sources, and an accepted suitable method for the automatic processing of large amounts of data. Its advantages are that it does not require a great deal of prior information (such as physical parameters), and it can quickly calculate the central depths

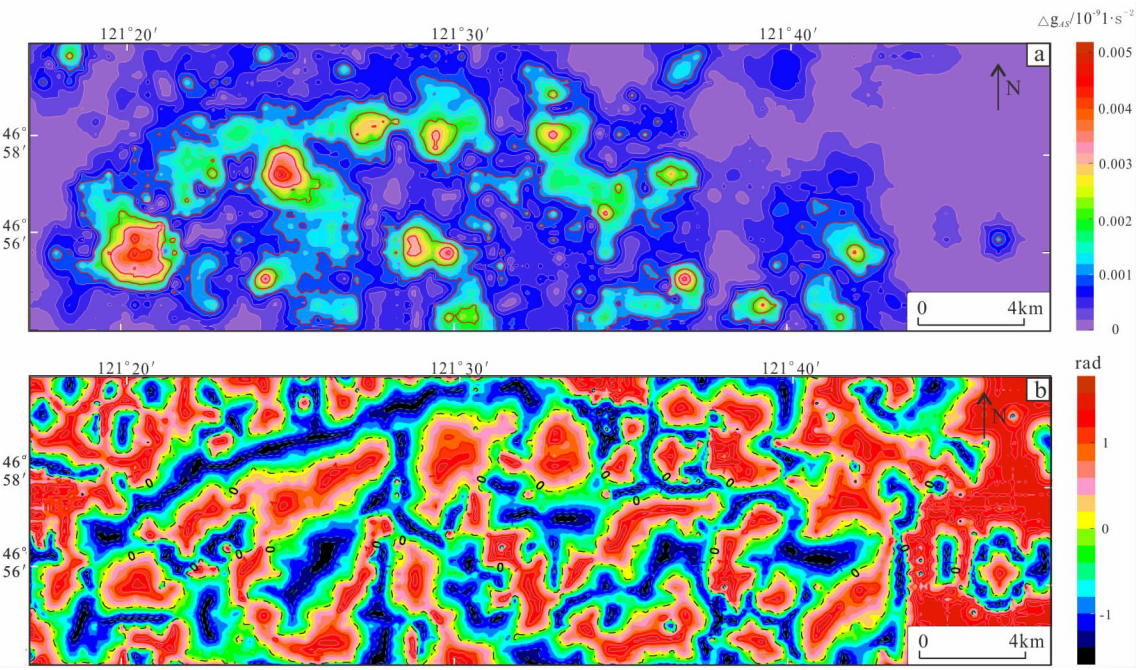

Fig. 4 Diagrams of total gradient modulus (a) and tilt angle results of local gravity anomalies (b)

of field sources. During the early stages of exploration, this method was found to be very helpful in the understanding of field source depths.

The gravity and magnetic anomalies satisfied the following Euler homogeneous equation:

$$f(x,y,z) = \frac{E}{r^N} \tag{6}$$

The partial differential equation of the Euler homogeneous equation could be expressed as follows:

$$(x-\xi_0)\frac{\partial f}{\partial x} + (y-\eta_0)\frac{\partial f}{\partial y} + (z-\zeta_0)\frac{\partial f}{\partial z} = -Nf \tag{7}$$

Where N represents the tectonic index. In regard to the gravity data, this study set N = 0, and the field sources were regarded as lithologic contact surfaces, geological body boundaries, or step models. A sliding window method was used to extract a small area of gravity data. Then, the data in the window were substituted into Equation (7) to form a group of equations. An Eulerian solution could then be obtained by solving the over-determined equations. Many of the Eulerian solutions could be calculated using the sliding window method in turn in accordance with the sliding step sizes. Finally, the final results were obtained by screening the solutions according to the dispersion criterion. Under normal circumstances, the Eulerian solutions will reflect the depths of the centers of the field sources (Wang, 2014; Ma *et al.*, 2013; Li & Yang, 2009). In this study, Euler deconvolution processing was applied to the Bouguer gravity anomaly following the reduction of the curved surfaces into a horizontal plane, and the results are shown in Fig. 5.

As they can be seen in Figs. 1 and 5, the Euler solutions were mainly distributed at the boundaries of the geological bodies. Overall, the regional structures were identified to mainly be NE-trending, as well as locally near the SN-trending. The majority of the field sources were shallowly buried within a depth of 1 km.

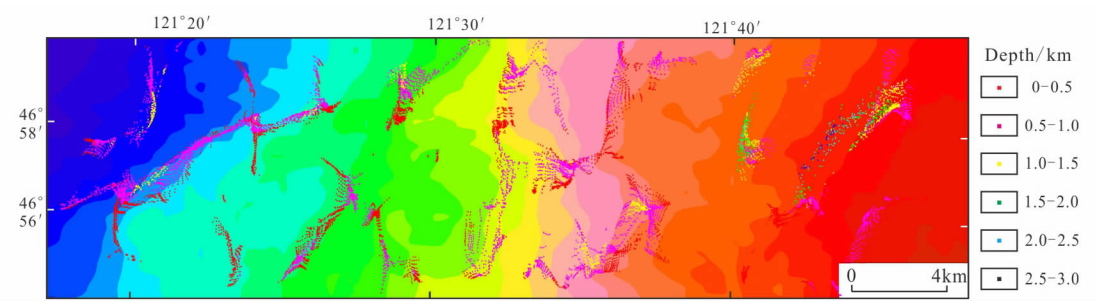

Fig. 5 Euler deconvolution results diagram of gravity anomaly (N = 0)

2.6 Divisions of the fault structures

In the current study, based on the previously mentioned data processing results, along with geological maps etc., four major faults and six secondary faults were identified in the study area. The results are shown in Fig. 6. It was determined that the main fault F1 intersected with F2. The F1 main fault was also cut by a secondary fault f_1, and the F4 main fault was be dissected by secondary faults f_2, f_3 and f_4, with the f_4 secondary intersecting with the f_5 and f_6 secondary faults, as detailed in Fig. 6.

As shown in Fig. 6, the bottom map refers to the Bouguer gravity anomaly map. Among the identified faults in the study area, the extension direction of the F1 fault was defined to be in the NE direction. This was mainly inferred from the boundary of the Bouguer gravity anomaly and the gradient zone of the Bouguer gravity anomaly. This was also confirmed to be the axis of the maximum horizontal derivative of the Bouguer gravity anomaly, as well as the dense area of Euler solution (N = 0) of Bouguer gravity anomaly at an elevation of 1 000 m following the reduction of the curved surfaces into a horizontal plane (Dai & Qu, 2009). The extension direction of the F2 fault was defined to be SN, which was inferred from the boundary of the Bouguer gravity anomaly. Also, it was the gradient

zone of the Bouguer gravity anomaly and the axis of the maximum value of the total horizontal derivative of the Bouguer gravity anomaly. The extension direction of the F3 fault was determined to be in a NNE direction, which is mainly inferred from the gradient zone of the Bouguer gravity anomaly and the maximum axis of the total horizontal derivative of the Bouguer gravity anomaly. The extension direction of the F4 fault was determined to be NNW, which was mainly inferred from the maximum axis of the total horizontal derivative of the Bouguer gravity anomaly and the dense area of the Euler solution ($N=0$) of the Bouguer gravity anomaly at an elevation of 1 000 m following the reduction of the curved surfaces into a horizontal plane. The secondary faults f_1 to f_6 are the processing results in this study.

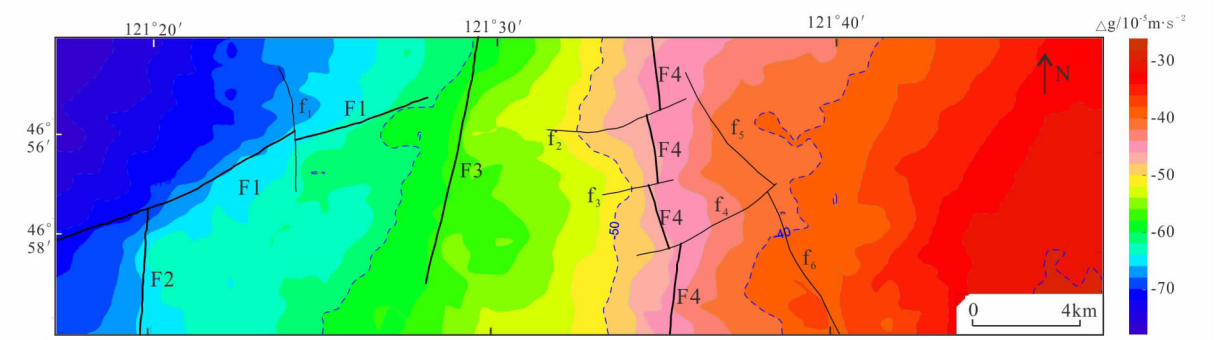

Fig. 6 Schematic map of fault structure divisions in the study area

3 Conclusions

In this study, several boundary identification methods, including horizontal derivative, vertical derivative, and total gradient modulus, were used to process the gravity data of the study area. The results provided basic data for a deeper understanding of the distributions of the fault structures. Then, by combining those results with the depth information of the faults obtained using the Euler deconvolution method, four main faults and six secondary faults were successfully identified in the study area. The findings of this study provided guideline for the future explorations of polymetallic ore veins. However, gravity anomalies are comprehensive responses of field sources with inhomogeneous density distributions in different depth ranges and scales. Therefore, the interpretation results may have multiple solutions and individual fault does not consistently match geological outcrop faults. Combinations of other geophysical methods may be required in the future to accurately analyze individual fault.

References

Chen A G, Zhou T F, Liu D J, *et al*. 2017. Application of the improved filter based on the Theta method to edge detection of potential field data: an example from the Luzong ore district. *Chinese Journal of Geophysics*, **60**(2): 778-792. (in Chinese with English abstract)

Dai M G, Qu S L. 2009. Determination of faults using gradient modules of potential field anomalies and its application to carbonate. *Progress in Geophysics*, **24**(3): 951-958. (in Chinese with English abstract)

Li C H. 2017. Processing and interpretation of magnetic data in Jirigen forest area in Xin'an League of Inner Mongolia: master's degree thesis. Changchun: Jilin University. (in Chinese with English abstract)

Liu Y F, He Z H, Gao L F, *et al*. 2018. Age, geochemistry and tectonic setting of granites from Huangtudaban in Suolun area, Inner Mongolia. *Global Geology*, **37**(3): 761-776. (in Chinese with English abstract)

Li Y F, Zhang F X, Zou Z H, *et al*. 2018. Normalized full gradient of gravity based on derivative-iteration method. *Global Geology*, **37**(1): 224-231. (in Chinese with English abstract)

Li Y Y, Yang Y S. 2009. Derivative-based normalized standard deviation of potential field data in geological contact mapping. *Geological Science and Technology Information*, **28**(5): 138-142. (in Chinese with English abstract)

Ma G Q, Du X J, Li L L, *et al*. 2013. New edge detection method of potential field data-enhanced horizontal deriva-

tive method. *Progress in Geophysics*, **28**(1): 402-408. (in Chinese with English abstract)

Ren J L, Zhang N, Wu Y G, *et al*. 2017. Interpretation of low-altitude aeromagnetic data in Duobaoshan mining area. *Global Geology*, **36**(4): 1252-1257. (in Chinese with English abstract)

Wang X P. 2014. Potential field characteristics and tectonic division in Dasanjiang region: master's degree thesis. Changchun: Jilin University. (in Chinese with English abstract)

Xiao F, Li L, Tian M Y, *et al*. 2018. Report on geophysical survey in Jirigen Forest Farm of Inner Mongolia. Changchun: Jilin University. (in Chinese)

Xu M L, Yang Y B, Wu Y G, *et al*. 2018. Zero-drift coefficient algorithm of gravimeter based on fuzzy weighted linear regression. *Global Geology*, **37**(3): 891-896. (in Chinese with English abstract)

Zhang N, Jia S, Jiang B, *et al*. 2017. Application of high-accuracy and low-altitude aeromagnetic survey in the volcanic tectonic area. *Mineral Exploration*, **8**(5): 881-888. (in Chinese with English abstract)

Zhang W D. 2015. Research on Late Jurassic volcanic institutions in Jirigen forest area, Zalaite Banner, Inner Mongolia. *Science*, *Technology and Enterprises*, (3): 130. (in Chinese)

Zhou X, Yu P, Weng A H, *et al*. 2018. Parallel forward modelling algorithm with gravity and gravity gradient data based on MPI and Open MP. *Global Geology*, **37**(3): 897-904. (in Chinese with English abstract)